

pubs.acs.org/cm Methods/Protocols

Rapid Identification of Synthetic Routes to Functional Metastable Phases Using X-ray Probed Laser Anneal Mapping (XPLAM) Time— Temperature Quench Maps

Robert T. Bell,*,[⊥] Peter A. Beaucage,*,[⊥] Marc J. Murphy,[⊥] Aine B. Connolly, Ulrich Wiesner, David Ginley, R. Bruce Van Dover, and Michael O. Thompson



Cite This: https://doi.org/10.1021/acs.chemmater.0c04926



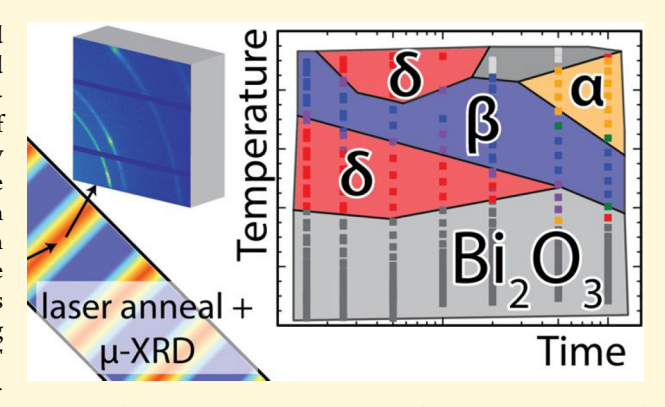
ACCESS

III Metrics & More

Article Recommendations

Supporting Information

ABSTRACT: Many material systems have known or predicted functional phases that are metastable at standard temperature and pressure. While substantial advances have been made in the high-throughput and combinatorial *synthesis* of materials with a range of stoichiometries, investigation of thermal processing remains largely the domain of iterative uniform anneals or static gradients. Here we develop X-ray probed laser anneal mapping (XPLAM), a high throughput technique coupling spatially resolved X-ray diffraction with microsecond to millisecond laser gradient anneals to produce temperature—dwell—transformation (TDT) diagrams of the phase as a function of quench time and temperature. In addition to showing regimes where specific metastable phases form preferentially, TDT diagrams provide insight into the submillisecond kinetics of solid—



solid phase transitions. This is a unique tool for mapping reaction pathways for metastable phases. As a first demonstration of XPLAM, we study Bi_2O_3 , which has a rich set of polytypes, including the δ -phase with an exceptionally high oxygen ion conductivity. We demonstrate the first annealing-driven synthesis of room temperature δ -Bi₂O₃. We expect XPLAM to prove a powerful technique for rapid identification of synthetic routes to metastable phases and to generate the exhaustive data sets required for machine learning-guided exploration of materials processing.

■ INTRODUCTION

Laser spike annealing (LSA) is an annealing technique in which a continuous laser beam is scanned rapidly across a sample (Figure 1A) resulting in microsecond to millisecond anneals. The unique capabilities of LSA have been applied for decades in the semiconductor industry to activate dopants¹, and have recently found wider adoption controlling phase changes, 3,4 nanoconfined crystal growth, 5,6 and prenucleating crystalline grains while limiting growth.⁷ The temporal heating profile in LSA is dependent on a number of factors, both process and material. For consistency, the duration of the laser anneal is referred to as the dwell, which is defined by dividing the full width at half max (fwhm) of the laser beam intensity profile in the scanning direction by the speed at which the laser is moving relative to the substrate. The peak temperature is a function of multiple parameters including the laser power, scanning speed, and sample substrate and is limited only by the thermal shock resistance of the substrate, with anneals on silicon possible to temperatures above the melting point at 1414 °C. The peak quenching rate is largely dependent on the peak temperature and the dwell, as shown in a comparison of 150 μ s and 2 ms dwells in Figure 1B,C. For example, at a 150 us dwell and 900 °C peak temperature, the peak quench rate

exceeds 10^6 °C s⁻¹, orders of magnitude faster than conventional furnace and rapid thermal processing techniques. We recently developed a lateral gradient laser spike anneal (lgLSA), which uses a bi-Gaussian focused laser beam during LSA to generate an anneal with a peak temperature gradient across the sample orthogonal to the laser scanning direction (Figure 1A).⁸ Due to the geometry of the laser focus, every point across a single lgLSA scan has the same dwell, even as peak temperature changes laterally. In addition, by focusing the beam to a fwhm of 600 μ m orthogonal to the scanning direction, the full width of an lgLSA scan is limited to 2 mm to 3 mm, allowing dense sampling of the dwell time and peak temperature conditions on relatively small samples by performing multiple scans on a single sample.

Received: December 28, 2020 Revised: May 21, 2021



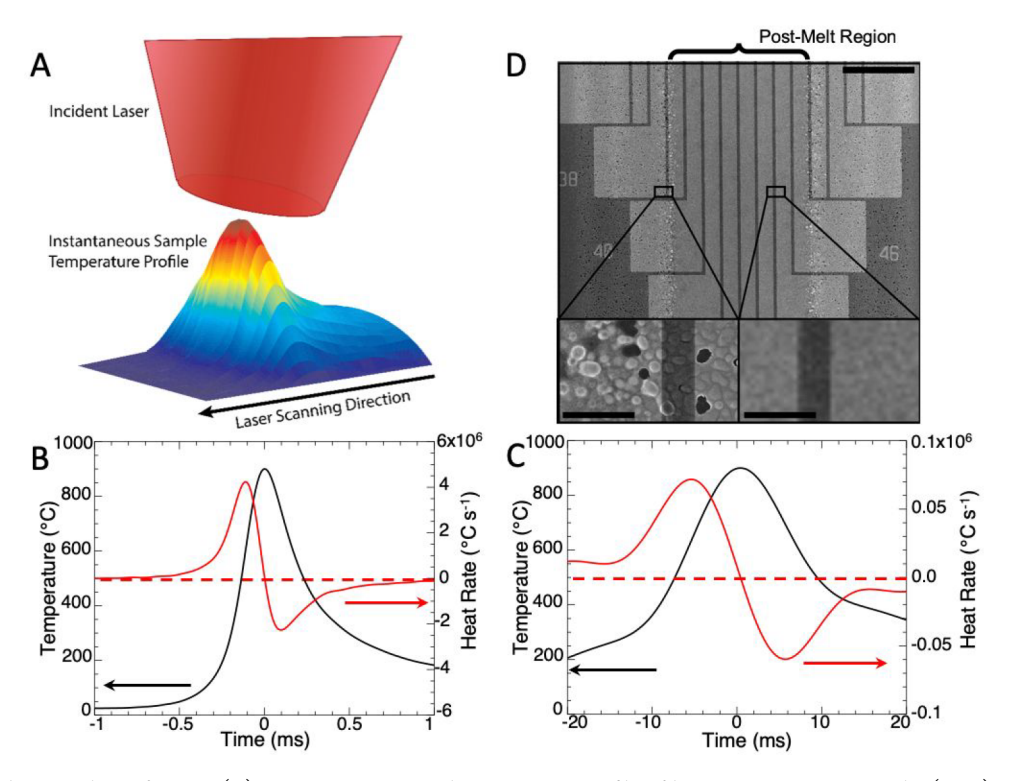


Figure 1. Laser spike annealing of Bi_2O_3 . (A) Instantaneous spatial temperature profile of laser scanning over sample. (B, C) Time, temperature, and heating rate profiles for a 0.15 ms (B) and 2 ms (C) dwell anneal with peak temperatures of 900 °C and peak quench rates of $\approx 2 \times 10^6$ °C s⁻¹ (B) and $\approx 7 \times 10^4$ °C s⁻¹ (C). (D) SEM of electrical contacts patterned on top of the 1 ms dwell annealed Bi_2O_3 film showing the pinhole-free postmelt region in the center bounded by regions with peak temperature below the melt on either side of the center (scale bar 100 μ m). Insets are magnified views of both postmelt and submelt regions (scale bars 10 μ m).

Here we develop X-ray probed laser anneal mapping (XPLAM), a powerful technique enabling the systematic high-throughput exploration of phase behavior as a function of annealing conditions. XPLAM combines the range of conditions generated by lgLSA with spatially resolved synchrotron X-ray diffraction (XRD) and phase analysis to quickly generate maps of phase as a function of temperature and dwell, which we term temperature—dwell—transformation (TDT) maps. TDT maps are analogous in many ways to classic temperature-time-transformation maps used for, among other things, guiding the complex processing of steels. Advances in both conventional computational materials design techniques and new, machine learning-guided tools have led to identification of ever-increasing numbers of candidate functional metastable materials.9 However, many metastable polymorphs are only accessible through specific reaction pathways, 10 requiring optimization of both the deposition and the processing parameters. Such routes to generate these metastable materials are unknown in most cases, and while materials with the correct chemistry can be deposited using a wide variety of combinatorial techniques, exploration of processing routes to produce the phase of interest is generally a highly manual process relying on individual anneals or static temperature gradients. One advantage of the short duration laser anneal processing is that points on the sample are spatially and kinetically isolated from interactions and compositions nearby, as opposed to more conventional static gradient annealing or composition gradient studies. This allows the time and temperature processing conditions leading to specific phases or reaction pathways to be identified with high certainty, with a wide range of conditions captured by multiple

laser anneals separated by millimeters, each possessing a full temperature gradient and unique annealing duration. In this work, we demonstrate the utility of this XPLAM technique and the generated TDT maps to identify deep knowledge on phase transformations and synthetic routes to metastable materials, using the example material system of $\mathrm{Bi_2O_3}$, with rich polymorphism and a functional phase inaccessible through conventional annealing. In particular, we demonstrate the first reported direct thermal processing synthesis of room temperature $\delta\text{-Bi_2O_3}$, where the $\delta\text{-phase}$ of $\mathrm{Bi_2O_3}$ is a defective fluorite phase with exceptionally high oxygen ion conductivity in its stable regime between 680 °C and the melting point at 830 °C. Below 680 °C, the $\delta\text{-phase}$ is metastable and the monoclinic $\alpha\text{-phase}$ becomes the stable phase.

Direct quenching of the δ -phase from high temperatures has been explored at quench rates up to 10 °C min^{-113,14} but always resulted in transformation below 600 °C to either the low temperature stable α -phase or metastable β - or γ -phases, all with substantially lower conductivities, ^{13–16} leading to the general consensus that thermal quenching of δ -Bi₂O₃ to room temperature is impossible. ^{17,18} A range of approaches have been attempted to preserve or duplicate the high oxygen-ion conductivity of δ -phase Bi₂O₃ at low temperatures. Stabilization of the δ -phase by alloying with heavy metals has been demonstrated ^{15,19,20} but results in dramatically reduced oxygen-ion conductivities compared to pure δ -Bi₂O₃. While direct low-temperature synthesis of δ -Bi₂O₃ has been reported using a variety of synthesis techniques, ^{20–23} the conductivity of δ -Bi₂O₃ has not been reported below 350 °C, ²¹ likely due to poor film quality or phase purity of directly synthesized

Table 1. Sample and Laser Annealing Conditions for Each Laser Scan Used in This Work

laser dwell ± 1%	peak temperature (°C) ± 10 °C	laser scanning speed $(m/s) \pm 0.001 \text{ m/s}$	laser power (W) ± 0.1 W	scan relative order (#1 = closest to wafer center)	lateral displacement of scan center from water center (mm) \pm 0.002 mm	film thickness (nm) ± 10 nm
150. μs	895 °C	0.6	54.9	#7	45.000	93
250. μs	903 °C	0.36	48.6	#5	40.000	123
500. μs	914 °C	0.18	41.7	#3	35.000	153
1.00 ms	926 °C	0.09	36.5	#2	32.500	168
2.00 ms	901 °C	0.045	33.3	#6	42.500	108
5.00 ms	932 °C	0.018	29.7	#1	30.000	183
10.0 ms	911 °C	0.009	28.6	#4	37.500	138

 $\delta\text{-Bi}_2O_3$. We speculate that such issues have also prevented the application of room temperature $\delta\text{-Bi}_2O_3$ in devices.

We map the resultant phases in the Bi₂O₃ system for annealing temperatures between room temperature and 900 °C (above the 830 °C equilibrium melting point) and dwell times between 0.15 to 10 ms (peak quench rates on the order of 10⁶ °C s⁻¹ and 10⁴ °C s⁻¹, respectively, Figure 1B,C), a regime well beyond that previously explored for Bi₂O₃ by any other method. By starting with amorphous Bi₂O₃ (Figure S1) with a high free energy, the driving force for nucleating an initial crystalline phase is much larger than the driving force for subsequent crystal-crystal transformations, allowing the limited kinetics of a short anneal to capture even the first nucleated phases. At temperatures that exceed the melting point, these anneals erase as-deposited film defects (Figure 1D), resulting in pinhole-free films. Fabrication of devices based on δ -Bi₂O₃ requires such pinhole-free films, and the creation of this quality of film with melt-processing provides a great deal of flexibility for postprocessing, regardless of the deposition method.

MATERIALS

Bi₂O₃ films were sputtered from a metallic Bi target (atomic fraction Bi > 99.99%) in an argon and oxygen plasma onto silicon wafers (p type, 0.01 Ω cm, WRS Materials) with a 117 nm typical thermal SiO₂ buffer layer (grown in a dedicated SiO₂ growth furnace; the samples for area anneals in Figure S5 used thinner buffer layers). The substrate was unheated during sputtering, and the as-deposited Bi₂O₃ was amorphous (Figure S1). The Bi₂O₃ thickness for all films in this study was within the range 90 to 190 nm (measured using profilometry) to minimize perturbations to the laser annealing. No thicknessdependent variations in phase formation of the as-deposited films were observed within this range. The thermal SiO₂ buffer layer between the silicon wafer and Bi₂O₃ was used to prevent melt alloying with the silicon wafer for laser scans where temperatures exceed the 830 °C Bi₂O₃ melting temperature. Melt alloying of Bi₂O₃ and SiO₂ is known to precipitate a stable body centered cubic bismuth silicate phase with a melting point near 900 °C at low silicon concentrations; ^{24,25} this phase was not observed for melt anneals in this study. On the ≤10 ms single anneal time scales used in this work, the SiO₂ buffer layer appears to prevent or minimize alloying of the Bi₂O₃ films even during melt.

LASER ANNEALING

Laser spike annealing was performed by scanning a continuous $10.6~\mu m$ wavelength line-focused CO_2 laser (as described previously⁸) across the sample, as shown in Figure 1a. The laser was focused into a bi-Gaussian shape with a full width at

half-maximum (fwhm) of 90 μ m in the scanning direction and 580 μ m in-plane orthogonal to the scanning direction. The dwell time, a measure of annealing duration, is defined as the fwhm of the laser intensity profile in the scanning direction divided by the scanning speed. The stage scanning speed was controlled to give a certain dwell, while the laser power was controlled to give a particular peak temperature. All anneals were performed in air. A preanneal over the entire sample area was performed, consisting of overlapping laser scans with a 400 $^{\circ}$ C peak temperature (18.4 W) at a 2 ms dwell with 10 μ m center-to-center spacing. These preannealing conditions were chosen due to the nucleation temperature across all measured dwells, and the preanneal was intended as a caution to drive out trapped Ar from the sputtering processes. A number of details for each single laser scan annealing condition in this work are given in Table 1. Temperature evolution as a function of time across the entire scan width was calibrated using micrometer scale platinum thermistors on matching Si substrates measured as described previously.8 The thermistors used to calibrate the temperature have dimensions of 2 μ m in the scanning direction (\approx 2% of the fwhm of the laser intensity profile in the scanning direction) and have a 4-point design to remove contact resistance from measurements. We measure the resistance of these thermistors at ≥500 kHz, which gives the temporal resolution of $\approx 2 \mu s$. The peak temperature experienced across the laser scan width was calibrated for each dwell and in all cases was approximately Gaussian with a maximum temperature near 900 °C and a fwhm of \approx 600 μ m, with longer dwells resulting in wider fwhm's. All Bi₂O₃ experiments were performed on identical silicon substrates to those used in calibrating the temperature. The Bi₂O₃ thickness dependent perturbation to the surface temperature was <2% as calibrated by Bi₂O₃ and Au dot melts⁸ for the <200 nm thick films used in this work. Laser scans create a line of annealed material where annealing conditions are invariant along the scan length but vary across the scan width. This allows the use of high aspect ratio rectangular areas for X-ray diffraction, with large areas of comparable annealing conditions despite the steep temperature gradient across the scan width. On the same sample, multiple separated scans were made with dwells of 0.15 to 10 ms with peak temperatures at the scan centers near 900 °C and with center-center separations of 2.5 mm. This allowed high throughput measurements of annealing times and temperature conditions on a single sample using spatially resolved measurements. To prevent systematic errors involving the film thickness, the order in which varying dwell laser scans were made was randomized, with the order given in Table 1. However, no evidence of systematic influence from the film thickness was observed.

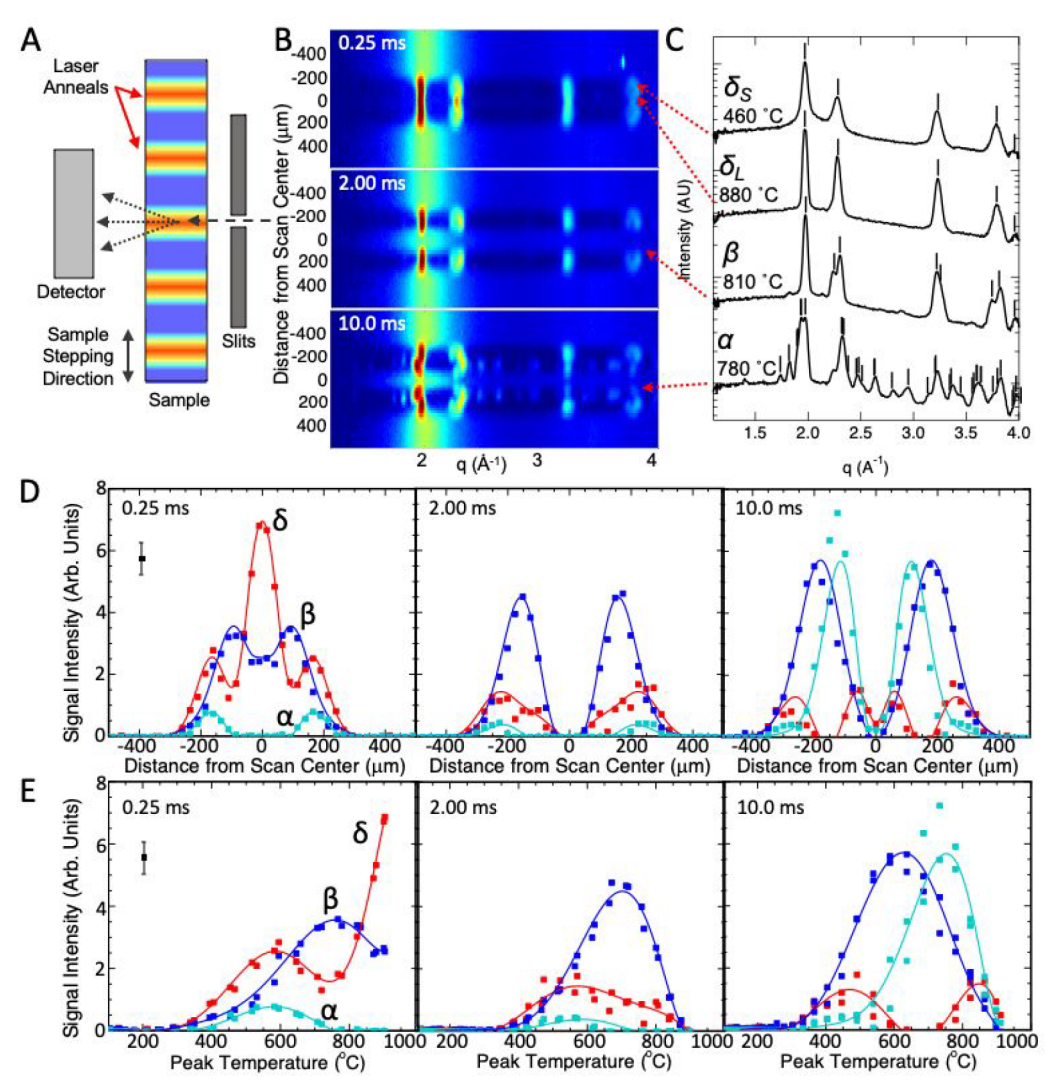


Figure 2. Mapping spatial- and temperature-dependent phase formation for different annealing dwell times. (A) Schematic of XPLAM method, showing X-ray microbeam mapping of the laser annealed sample. The incident X-ray beam (dashed, 25 μm wide after slits) is parallel to the laser annealed regions. Diffraction patterns are taken across varying peak temperature and dwell conditions as the sample is stepped. (B) Heat maps of diffraction intensity, I(q), as a function of spatial location across lgLSA scans for dwells of 0.25, 2.00, and 10.0 ms with 900 °C peak temperatures in the scan centers. (C) Diffraction patterns for resultant δ (cubic; nucleated by transformations solid → solid, δ_S , shown with peak temperature 460 °C and liquid → solid, δ_L , shown with peak temperature 880 °C), β (tetragonal, shown with peak temperature 810 °C), and α (monoclinic, shown with peak temperature 780 °C) phases with arrows marking their location in (B). (D) Relative diffraction intensities for δ (red), β (blue), and α (teal) phases across each lgLSA scan in (B). A typical least-squares fitting error bar is shown in black in the 0.25 ms figure. Solid lines are symmetric fits. Note that, though the fitting routine produces intensities above zero for all phases at all points, the XPLAM process frequently produces phase-pure materials, e.g., the patterns in (C) and regions in Figure 3 (vide infra). These small reported contributions of, for example, β to phase-pure δ , reflect numerical uncertainty and the similarity of the two phases rather than physical reality. (E) Intensities from (D) converted from location to calibrated peak temperature.

X-RAY DIFFRACTION

X-ray diffraction measurements were conducted ex situ at station G1 of the Cornell High Energy Synchrotron Source (CHESS). The X-ray beam was reduced to a 25 $\mu m \times 200~\mu m$ rectangle using a standard three-slit setup. The sample was mounted in a near-grazing-incidence configuration (angle of incidence $\omega=3^{\circ}$) and aligned such that the temperature gradient across the laser scans was orthogonal to the incident beam, allowing diffraction measurements to be spatially indexed to a precise temperature (area averaging over the gradient resulting in a range of 0 to 50 °C temperatures captured in each measurement, depending on the temperature gradient at that point) and dwell annealing conditions. Laser anneals were aligned to be parallel to the flat of the Si substrate

wafers, which allowed facile X-ray alignment performed to the wafer flat (transmission mode, wafer blocking, $\omega=0^\circ$) to be used as alignment to the laser anneals. The low angle of incidence was chosen to optimize the vertical beam footprint on the sample while simultaneously allowing diffraction to be captured. The incident X-ray beam energy was 9.81 keV, and the typical sample—detector distance was 20 cm; precise sample—detector distances were calibrated using copper tape adhered to each end of each sample and linearly interpolated where necessary between the two reference points due to wafer tilt. The small sample—detector distance used in these studies makes such corrections important since uncertanties of a few millimeters in the sample—detector distance propagate to several percent uncertainties in the scattering vector. The

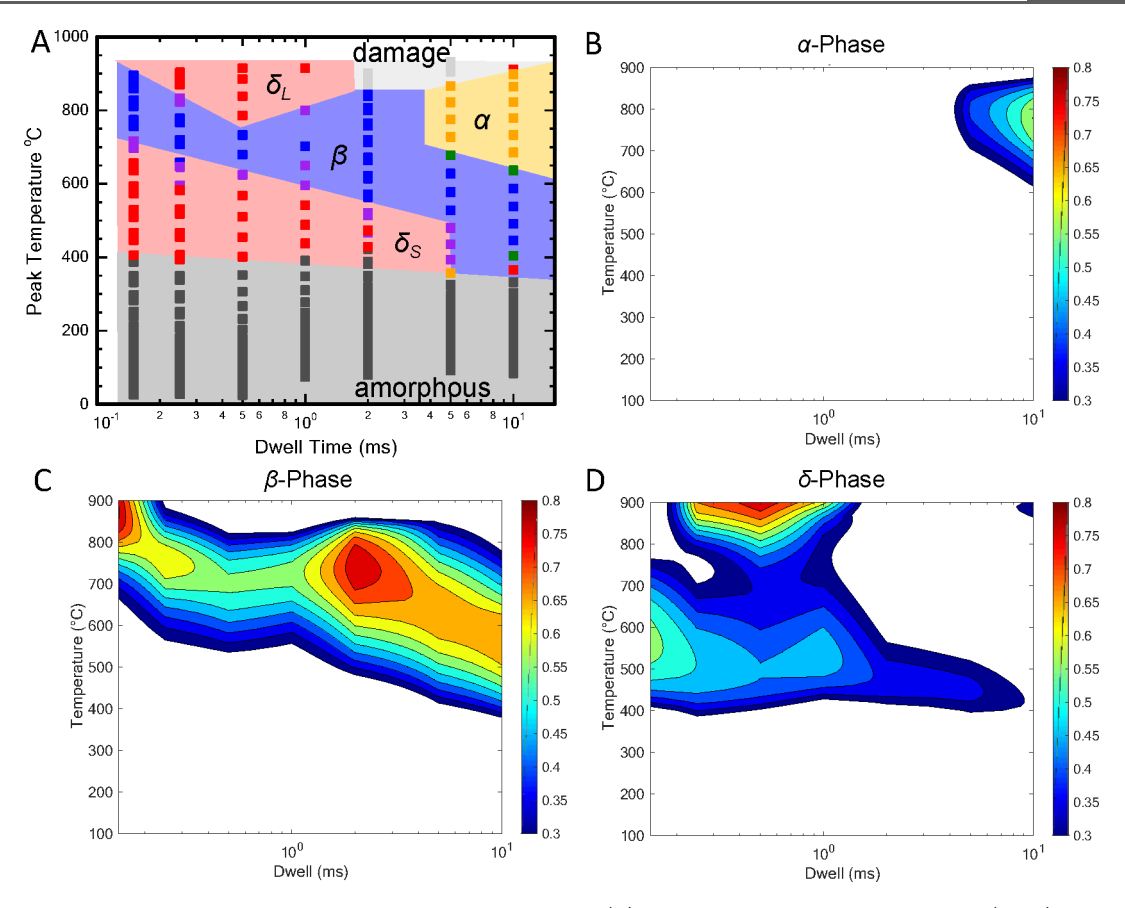


Figure 3. Peak annealing temperature and dwell time maps of Bi_2O_3 phases. (A) Temperature—dwell—transformation (TDT) diagram displaying the predominant room temperature phase as a function of dwell time and peak temperature: δ , red; β , blue; α , yellow; mixed α/β , green; mixed δ/β , purple; amorphous, dark gray; and damage, light gray. Each square is a measured condition, and colored regions indicate the approximate processing regimes expected to result in each phase. (B–D) Weighted phase fractions of the room temperature stable α -phase (B), β -phase (C), and δ -phase (D).

amorphous SiO_2 peak near 3 Å⁻¹ (Figure S1) was uniform across all measurements and was subtracted from the diffraction patterns shown here for clarity.

MAPPING PHASE FORMATION

XPLAM (Figure 2A) was used to map phase development across samples. Spatial maps (Figure 2B) of diffraction patterns were taken using a 25 μ m wide X-ray beam for select dwells of 0.25, 2, and 10 ms and show the transition from amorphous at low peak temperatures (edges) to crystalline at higher temperatures (centers). Peak-splitting at 2 Å⁻¹, 2.3 Å⁻¹, and 3.8 Å^{-1} indicates formation of multiple phases as a function of peak temperature and dwell. Damage, likely due to partial reduction and evaporation of molten Bi₂O₃, is observed for peak temperatures above the 830 °C equilibrium melt for longer dwells of 2, 5, and 10 ms and manifests in the XRD results as an amorphous region with a slightly lower q peak center than the as-deposited films (see centers of 2 and 10 ms scans in Figure 2B). Characteristic diffraction patterns for α , β , and δ (designated as δ_S when formed from the solid phase and δ_L when formed from the melt) are given in Figure 2C, where peak markings correspond to Inorganic Crystal Structure Database (ICSD) entries for the phases, including compensation for the peak shift likely induced by lattice strain. The contribution of each phase to the measured diffraction was identified as a function of the position (Figure 2D) and peak temperature (Figure 2E) using a basic fitting routine. It should

be noted that though the representative curves in Figure 2D reflect some contribution of all phases at all points, the XPLAM technique does produce phase-pure materials, e.g., the points highlighted in Figure 2C. The mixed-phase fits in Figure 2D are reflective of numerical uncertainty in comparing very similar diffraction traces, not overwhelming mixed phase behavior.

By identifying the dominant phase for each peak temperature at seven dwells between 0.15 and 10 ms, a TDT diagram was constructed (Figure 3A). Processing regimes resulting in the same dominant phase are identified. The film remains amorphous for temperatures below 350 to 400 °C for all dwells investigated. Above these temperatures, the fractional intensity of each phase was mapped (Figure 3B-D). While regions of both multiple phases and single phases are observed in the XRD patterns (Figure 2B,C), Figure 3B–D underestimates the phase purity of the dominant phase, resulting in no identification of "single-phase" regions. This is due to complications of the diffraction measurement: the microbeam size scale decreases the signal-to-noise ratio of the XRD, the silicon substrate contributes a thermal diffuse scattering background, the amorphous SiO₂ underlayer contributes background, and there is substantial overlap of the Bi₂O₃ polymorphs' diffraction peaks, especially at small grain sizes such as when nucleating from the amorphous phase. The multipeak fitting used in this work fits the several highest intensity peaks of each phase, described further in the SI, and

uses comparisons of the relative intensities of the highest intensity peak of each phase to generate Figure 3B-D. However, a combination of the above factors causes the phase identification to assign some intensity contribution to Bi₂O₃ amorphous, α , β , and δ -phases in most cases and, thus, underestimates phase purity of the dominant phase. It is possible that a combination of more advanced peak fitting and strategies to reject the thermal diffuse background could be developed to better differentiate these phases. However, from the representative diffraction patterns shown in Figure 2C, it is clear that some regions do in fact produce a phase pure δ -phase. To verify the generation of the phase-pure material, we collected microbeam Raman spectra at selected points in a laser scan (Figure S2). Two phase-pure δ -phase forming regimes are identified, one via a solid-state transformation (δ_s) in a shrinking temperature window ranging from just above the amorphous transition to 750 °C at 150 μ s and 500 °C at \leq 5 ms and the other via a melt mediated transformation (δ_L) for temperatures above \approx 750 °C and dwells below 2 ms. A β -rich region is found between high and low temperature δ -phase regions and extends to 10 ms, and an α -rich region appears at the longest dwells and highest temperatures.

The resulting δ -phase differs between the δ_s - and δ_t -regions in two key fashions: remnant amorphous fraction and grain size. We believe the low temperature δ_S regime is the result of a direct amorphous to δ transformation, as evidenced by a remnant amorphous Bi₂O₃ fraction that appears as a broad peak near 2 Å⁻¹ for δ_S shown in Figure 2c as well as the absence of other crystalline phases. The lower temperature of the $\delta_{\rm S}$ region likely depresses the kinetics of grain growth, consistent with the remaining amorphous fraction. Additionally, $\delta_{\rm S}$ exhibits small grain sizes consistent with a large concentration of nucleation sites, likely due to variation in local density and stress in the as-sputtered amorphous phase. In contrast, we believe that the δ_L -region is a result of nucleation from melt during quench, with the lower bound of the δ_L -region likely depressed to the observed 750 °C from the 830 °C equilibrium melting point as a result of a glass transition from the starting metastable amorphous state. The δ_L -region exhibits several characteristics of nucleation from the melt, namely, large grain sizes (scattering domains > 100 nm by Debye-Scherrer analysis) which are on the order of the full film thickness. These large grains are likely the result of nucleation-limited growth driven by a combination of a few nucleation sites (in this case homogeneous nucleation sites removed during the melt) and rapid grain growth kinetics in the near-melt supercooled liquid. This δ_L -region likely heterogeneously nucleates during quench from the top or buried interfaces. Interestingly, while the two-dimensional diffraction patterns for α , β , and δ_S exhibit very little anisotropy (Figure S3a-c), the δ_{τ} region exhibited spots consistent with textured crystal growth (Figure S3d). This texturing suggests that nucleation of δ_L is either governed by heterogeneous nucleation or that quenched liquid film generates a uniform stress state throughout the quenched region which prefers certain orientations of nuclei.

These transformation maps suggest that the δ -phase is the kinetically preferred phase to initially nucleate under most conditions, with the observed β - and α -phases forming as a result of a subsequent amorphous $\to \delta \to \beta \to \alpha$ transformation pathway, with the exception of the intersection of the shortest dwells and highest temperatures investigated where the β -phase appears to nucleate first. The presence of an

amorphous signal in short dwell δ_S strongly suggests that the δ phase nucleates first in solid state transformations. The β rich region between δ_S and δ_L largely overlaps the temperature region where δ is the equilibrium phase, which suggests that thermodynamics would favor δ nucleation. At dwells of 500 μ s and greater, we believe that the β -rich region results from an amorphous $\rightarrow \delta \rightarrow \beta$ transformation pathway, mimicking the rapid transformation of $\delta \rightarrow \beta$ at 650 °C widely reported in furnace quenches. 13 This hypothesis is supported by the inverse relationship between δ - and β -phase fractions as temperatures and dwells increase (Figures 3C,D and S4). In fact, the continued presence of δ to longer dwells at lower temperatures allows identification that the $\delta \rightarrow \beta$ nucleation rate maximum occurs between 550 and 650 °C. Observation of diffraction patterns at different dwells and with peak temperatures between 550 and 650 °C captures multiple snapshots of $\delta \rightarrow \beta$ transformation at varying phase fractions of δ and β corresponding to differing completeness of the transformation. These mixed-phase regions suggest that $\delta \to \beta$ transformation near 600 °C occurs over a time scale on the order of hundreds of microseconds, likely due to relatively slow kinetics of nucleating the β -phase and even slower kinetics of growth.

The presence of a local maximum in the β -composition at the shortest dwells and highest temperatures (where grain size of the β-phase remains \ll 100 nm in contrast to δ_L) is not fully explained by this model, suggesting that another factor may cause direct amorphous $\rightarrow \beta$ nucleation under these extreme conditions. We postulate two explanations for this regime: (i) heterogeneous nucleation sites persist to high temperatures due to the rapid heating rate or (ii) during the extreme quench from high temperature the sample passes through the nucleation window of the δ -phase too rapidly to form the δ-phase, leading to nucleation from a relaxed amorphous/ supercooled liquid directly into β -phase. Ultimately, the exact mechanism(s) behind formation of this short dwell at the high temperature β -phase region are difficult to identify with ex situ X-ray analysis, and other in situ, both X-ray and optical, metrology techniques during laser annealing are under development.

The lack of the very distinct α signal until 500 μ s dwells and high temperatures suggests that, despite being the stable phase at temperatures below 730 °C, α does not directly nucleate from the amorphous phase and is instead produced by an amorphous $\rightarrow \delta \rightarrow \beta \rightarrow \alpha$ transformation pathway. This mirrors the transformation pathway during furnace quenching from the high temperature stable δ -phase of $\delta \rightarrow \beta \rightarrow \alpha$. ^{13,18} The disappearance of both δ regimes by 10 ms dwells, where at 10 ms dwell the quench is near 10⁴ °C s⁻¹, explains why the quench of the δ -phase has not been previously accomplished by prior studies using much lower quench rates.

The δ -phase is preserved in melt processed films for dwells up to 1 ms, despite nucleation of β at submelt temperatures for dwells as short as 0.15 ms. These results suggest that melt processing substantially lowers the concentration of defects in the Bi₂O₃ film, reducing the number of nucleation sites, and subsequently depresses $\delta \to \beta$ nucleation rates compared to solid state processing. This also suggests that melt produced δ -films may have increased low-temperature stability compared to δ -films produced by other methods.

While this work focuses on nucleation from an initially amorphous film, similar experiments would also be possible with an initially crystalline film. Below the melting point of the

initial phase (suppressed from the equilibrium melting point if the film has substantial initial stresses and/or is initially a metastable phase), the nucleation pathways observed will be heavily dependent on the initial phase and may differ from what would be observed as first nucleating from the amorphous phase. An example of this relevant to the Bi₂O₃ system would be starting with a γ -phase sample; since the γ -phase is observed in certain slow furnace quenches of the δ -phase but is not observed in this work, beginning in the γ phase would be a way to study the transformation kinetics of that phase. In a TDT diagram beginning from a crystalline phase, dwells that enter the melt regime (for a sufficiently long dwell dependent on the material system) should erase any preference of the initial crystalline phase, and the results should match those of an amorphous film heated above the melt. For most material systems we anticipate that the TDT diagram would look the same above the melting point regardless of initial phase. The exception to this would be material systems where grain growth can occur at rates approaching the speed of sound in the medium, which would allow crystallites bordering the melt region to grow into the supercooled region during quench. This does not typically occur because of the distances (tens of micrometers) and time scales (micro- to milliseconds) of the quench. However, we predict that, in certain edge cases, such as certain pure metals, growth from bordering crystallites could strongly influence the TDT diagram.

Translation of TDT diagrams to large area anneals require overlapping LSA scans, staggered orthogonal to the scanning direction. This large area LSA technique is frequently used in the semiconductor industry to create large areas of uniform dopant activation, among other uses. Large area samples of δ-Bi₂O₃ were prepared using overlapped laser scans of conditions of a 900 $^{\circ}$ C peak temperature and 250 μ s, identified on the TDT map to generate δ_L . These overlapping scans do result in some reannealing δ -phase areas at lower temperatures, dependent on the scan spacing and the lateral temperature profile. However, since the δ_L region on the TDT diagram extends across a wide range of dwells, the effective dwell increase by overlapping scans still resulted in the δ -phase uniformly. However, the reannealing of δ -Bi₂O₃ in the large area sample does result in additional diffraction peaks that are consistent with simulations of oxygen-ordered δ -Bi₂O₃ (Figure S5), ²⁶ suggesting that partial oxygen vacancy ordering may be occurring for room-temperature δ -Bi₂O₃. These additional peaks are predicted to appear due the symmetry breaking of the fluorite structure as oxygen vacancies order on a supercell, and similar effects due to ordering of oxygen vacancies have been observed for dopant stabilized δ-Bi₂O₃. ^{26,27} We hypothesize that these additional peaks, present in the large area anneals but not apparent in the single lgLSA data, are due to domains of ordered oxygen vacancies that either nucleate or grow during the reannealing associated with overlapping LSA scans in the large area anneals.

CONCLUSION

In this work, we describe the execution of the XPLAM technique and demonstrate its utility by studying the model $\mathrm{Bi_2O_3}$ system. The TDT maps generated by XPLAM capture the kinetics of amorphous to solid, liquid to solid, and polytype to polytype transformations. We demonstrate this technique and the subsequent analysis on the model $\mathrm{Bi_2O_3}$ system with the promising functional phase $\delta\text{-Bi_2O_3}$. In this $\mathrm{Bi_2O_3}$ system we demonstrate for the first time synthesis of room

temperature δ -Bi₂O₃ through thermal processing and identify two distinct regions of synthetic conditions for δ -Bi₂O₃, one passing through melt and the other arising from nucleation from the amorphous phase. The effect of the synthetic route on the subsequent stability of δ -Bi₂O₃ is discussed, with melt processing resulting in a decreased rate of transformations to other polytypes when quenching from high temperatures, likely due to a decrease in heterogeneous nucleation sites in the melt processed films. We demonstrate that the low temperature stable α -phase does not nucleate directly from either the melt or the amorphous precursor film but rather is the product of a complex polytype to polytype transformation pathway following the route amorphous $\rightarrow \delta$ -phase $\rightarrow \beta$ -phase \rightarrow α -phase. From this work we were also able to identify the temperature region where nucleation rates of specific phases from specific metastable phases were maximized; for example, the nucleation rate of the β -phase from δ -Bi₂O₃ is maximized in the temperature regime from 550 to 650 °C. Finally, we discuss how synthetic conditions identified using XPLAM may be used to generate larger area samples.

The XPLAM technique is a powerful tool for rapidly generating understanding of the formation and evolution of metastable materials. The TDT maps created provide clear synthetic instructions for synthesizing any metastable materials that are formed, and in cases like this model system can provide guidance to high phase purity. Additionally, the technique provides insight into kinetics and transformation pathways. We believe that XPLAM is a valuable technique for investigating functional metastable materials as well as increasing understanding of even well studied material systems.

ASSOCIATED CONTENT

Supporting Information

The Supporting Information is available free of charge at https://pubs.acs.org/doi/10.1021/acs.chemmater.0c04926.

Detailed methods, diffraction data (including two-dimensional diffraction), Raman spectroscopy, X-ray photoelectron spectroscopy, and additional analysis of annealing data (PDF)

AUTHOR INFORMATION

Corresponding Authors

Robert T. Bell — Department of Materials Science and Engineering, Cornell University, Ithaca, New York 14853, United States; Materials Science Division, National Renewable Energy Laboratory, Golden, Colorado 80401, United States; orcid.org/0000-0003-0923-6012; Email: robert.bell@nrel.gov

Peter A. Beaucage — Department of Materials Science and Engineering, Cornell University, Ithaca, New York 14853, United States; Materials Science & Engineering Division and NIST Center for Neutron Research, National Institute of Standards and Technology, Gaithersburg, Maryland 20899, United States; orcid.org/0000-0002-2147-0728; Email: peter.beaucage@nist.gov

Authors

Marc J. Murphy – Department of Materials Science and Engineering, Cornell University, Ithaca, New York 14853, United States

- Aine B. Connolly Department of Materials Science and Engineering, Cornell University, Ithaca, New York 14853, United States
- Ulrich Wiesner Department of Materials Science and Engineering, Cornell University, Ithaca, New York 14853, United States; © orcid.org/0000-0001-6934-3755
- David Ginley Materials Science Division, National Renewable Energy Laboratory, Golden, Colorado 80401, United States
- R. Bruce Van Dover Department of Materials Science and Engineering, Cornell University, Ithaca, New York 14853, United States
- Michael O. Thompson Department of Materials Science and Engineering, Cornell University, Ithaca, New York 14853, United States

Complete contact information is available at: https://pubs.acs.org/10.1021/acs.chemmater.0c04926

Author Contributions

¹(R.T.B., P.A.B., and M.J.M.) These authors contributed equally to this work

Author Contributions

R.T.B. and M.J.M. proposed the study. M.J.M., R.B.v.D., and R.T.B. designed the deposition. M.J.M. deposited the samples. R.T.B. designed and ran the laser annealing. P.A.B. and R.T.B. designed and ran the X-ray experiments. R.T.B., M.O.T., and P.A.B. analyzed the X-ray data. P.A.B. measured and U.W. supervised the SEM experiments. M.J.M. performed and M.J.M. and P.A.B. analyzed the XPS experiments. A.B.C. performed and A.B.C., R.T.B., P.A.B., R.B.v.D., and M.O.T. analyzed the Raman experiments. R.T.B., P.A.B., and M.J.M. wrote the manuscript with input from all authors.

Funding

This work made use of the Cornell Center for Materials Research Shared Facilities which are supported through the NSF MRSEC program (DMR-1719875), the Cornell High Energy Synchrotron Source (CHESS) which is supported by the NSF (DMR-1332208), and the Cornell NanoScale Facility, a member of the National Nanotechnology Coordinated Infrastructure (NNCI), which is supported by the NSF (ECCS-1542081). This work was supported by the U.S. Department of Energy under Contract No. DE-AC36-08GO28308 with the Alliance for Sustainable Energy, LLC, the manager and operator of the National Renewable Energy Laboratory (NREL). Funding support for R.T.B. and D.G. was provided by the Department of Energy Office of Science, Office of Basic Energy Sciences, as part of the Energy Frontier Research Center "Center for Next Generation of Materials Design: Incorporating Metastability". R.T.B. was supported by the NSF GK12 fellowship program (DGE-1045513) and Kionix fellowship. P.A.B. was supported by the NSF Graduate Research Fellowship Program (DGE-1650441), by the U.S. Department of Energy, Office of Science Graduate Student Research program (DE-SC0014664), and by the NIST-NRC postdoctoral fellowship program. U.W. thanks the U.S. National Science Foundation under Award No. DMR-1707836 for support. M.O.T., R.B.vD., and A.B.C. thank the United States Air Force Office of Scientific Research for support under award numbers FA9550-18-1-0136 and FA9550-18-1-0529.

Notes

The authors declare the following competing financial interest(s): Cornell University has filed a patent based upon materials reported in this work, specifically the delta-phase of $\mathrm{Bi}_2\mathrm{O}_3$ synthesized using millisecond and sub-millisecond annealing.

Data will be made available upon request to corresponding authors.

ACKNOWLEDGMENTS

We thank A. Woll and H. Joress for assistance with equipment for synchrotron diffraction. Certain commercial equipment, instruments, materials, or software are identified in this paper to foster understanding. Such identification does not imply recommendation or endorsement by the National Institute of Standards and Technology, nor does it imply that the materials or equipment identified are necessarily the best available for the purpose.

REFERENCES

- (1) White, C. W.; Narayan, J.; Young, R. T. Laser Annealing of Ion-Implanted Semiconductors. *Science* **1979**, 204, 461–469.
- (2) Robinson, A. L. Laser Annealing: Processing Semiconductors Without a Furnace. *Science* **1978**, *201*, 333–335.
- (3) Orava, J.; Greer, A. L.; Gholipour, B.; Hewak, D. W.; Smith, C. E. Characterization of supercooled liquid Ge₂Sb₂Te₅ and its crystallization by ultrafast-heating calorimetry. *Nat. Mater.* **2012**, *11*, 279–283
- (4) Wuttig, M.; Yamada, N. Phase-change materials for rewriteable data storage. *Nat. Mater.* **2007**, *6*, 824–832.
- (5) Tan, K. W.; et al. Transient laser heating induced hierarchical porous structures from block copolymer-directed self-assembly. *Science* **2015**, *349*, 54–58.
- (6) Arora, H.; et al. Block Copolymer Self-Assembly-Directed Single-Crystal Homo- and Heteroepitaxial Nanostructures. *Science* **2010**, 330, 214–219.
- (7) Dabney, M. S.; et al. Altering the nucleation of thermally annealed hydrogenated amorphous silicon with laser processing. *Appl. Phys. Lett.* **2009**, *95*, 251902.
- (8) Bell, R. T.; et al. Lateral Temperature-Gradient Method for High-Throughput Characterization of Material Processing by Millisecond Laser Annealing. ACS Comb. Sci. 2016, 18, 548–558.
- (9) de Jong, M.; Chen, W.; Geerlings, H.; Asta, M.; Persson, K. A. A database to enable discovery and design of piezoelectric materials. *Sci. Data* **2015**, *2*, 150053.
- (10) Sun, W.; Dacek, S. T.; Ong, S. P.; Hautier, G.; Jain, A.; Richards, W. D.; Gamst, A. C.; Persson, K. A.; Ceder, G.; et al. The thermodynamic scale of inorganic crystalline metastability. *Sci. Adv.* **2016**, 2, No. e1600225.
- (11) McGinn, P. J. Thin-Film Processing Routes for Combinatorial Materials Investigations A Review. *ACS Comb. Sci.* **2019**, *21*, 501–515.
- (12) Khan, I. S.; Heinselman, K. N.; Zakutayev, A. Review of ZnSnN₂ semiconductor material. *J. Phys. Energy.* **2020**, *2*, 032007.
- (13) Harwig, H. A.; Gerards, A. G. The polymorphism of bismuth sesquioxide. *Thermochim. Acta* 1979, 28, 121–131.
- (14) Schröder, F.; Bagdassarov, N.; Ritter, F.; Bayarjargal, L. Temperature dependence of Bi_2O_3 structural parameters close to the α - δ phase transition. *Phase Transitions* **2010**, 83, 311–325.
- (15) Drache, M.; Roussel, P.; Wignacourt, J. P. Structures and oxide mobility in Bi-Ln-O materials: Heritage of Bi₂O₃. *Chem. Rev.* **2007**, 107. 80–96.
- (16) Bayliss, R. D.; Cook, S. N.; Kotsantonis, S.; Chater, R. J.; Kilner, J. A. Oxygen ion diffusion and surface exchange properties of the α and δ -phases of Bi₂O₃. *Adv. Energy Mater.* **2014**, *4*, 1301575.

- (17) Conflant, P.; Follet-Houttemane, C.; Drache, M. The Bi_2O_3 - Sm_2O_3 system: phase diagram and electrical properties. *J. Mater. Chem.* **1991**, *1*, 649–653.
- (18) Webster, N. A. S.; Ling, C. D.; Raston, C. L.; Lincoln, F. J. The structural and conductivity evolution of fluorite-type Bi₂O₃-Er₂O₃-PbO solid electrolytes during long-term annealing. *Solid State Ionics* **2008**, *179*, 697–705.
- (19) Borowska-Centkowska, A.; et al. Conductivity in lead substituted bismuth yttrate fluorites. *Solid State Ionics* **2014**, 254, 59–64.
- (20) Sanna, S.; et al. Enhancement of the chemical stability in confined δ -Bi₂O₃. *Nat. Mater.* **2015**, *14*, 500–504.
- (21) Laurent, K.; Wang, G. Y.; Tusseau-Nenez, S.; Leprince-Wang, Y. Structure and conductivity studies of electrodeposited δ -Bi₂O₃. *Solid State Ionics* **2008**, *178*, 1735–1739.
- (22) Switzer, J. A.; Shumsky, M. G.; Bohannan, E. W. Electro-deposited Ceramic Single Crystals. *Science* **1999**, 284, 293–296.
- (23) Takeyama, T.; Takahashi, N.; Nakamura, T.; Itoh, S. Growth and characterization of high-quality δ -Bi₂O₃ thin films grown by carbothermal evaporation. *Mater. Lett.* **2006**, *60*, 1733–1735.
- (24) Harwig, H. A.; Gerards, A. G. Electrical properties of the α , β , γ , and δ phases of bismuth sesquioxide. *J. Solid State Chem.* **1978**, 26, 265–274.
- (25) Levin, E. M.; Roth, R. S. Polymorphism of bismuth sesquioxide. II. Effect of oxide additions on the polymorphism of Bi₂O₃. *J. Res. Natl. Bur. Stand., Sect. A* **1964**, *68A*, 197.
- (26) Aidhy, D. S.; Nino, J. C.; Sinnott, S. B.; Wachsman, E. D.; Phillpot, S. R. Vacancy-ordered structure of cubic bismuth oxide from simulation and crystallographic analysis. *J. Am. Ceram. Soc.* **2008**, *91*, 2349–2356.
- (27) Wachsman, E. D. Effect of oxygen sublattice order on conductivity in highly defective fluorite oxides. *J. Eur. Ceram. Soc.* **2004**, *24*, 1281–1285.

I